

## Modeling the solar loading thermography inspection of structures with finite elements method

by B. Méthot\*, C. Ibarra-Castanedo\*, M. Klein\*\* and X. PV Maldague\*

\* Université Laval, 2325 Rue de l'Université, Québec, QC, Canada, [benjamin.methot.1@ulaval.ca](mailto:benjamin.methot.1@ulaval.ca), [clemente.ibarra-castanedo@gel.ulaval.ca](mailto:clemente.ibarra-castanedo@gel.ulaval.ca), [xavier.maldague@gel.ulaval.ca](mailto:xavier.maldague@gel.ulaval.ca)

\*\* Infrared Thermography Testing Systems, Visioimage Inc., Quebec City, QC G1W 1A8, Canada, [matthieu.klein@visioimage.com](mailto:matthieu.klein@visioimage.com)

### Abstract

Multiple non-destructive testing techniques, such as infrared thermography, have been used to inspect large structures and detect voids behind surfaces. Solar loading thermography is a technique that has been used experimentally but few models have been made to determine its theoretical potential. Finite elements models done with COMSOL show that under certain circumstances, voids located 1.5 meters below the visible surface may be detected in less than 20 days of continuous observation with an infrared camera, following lock-in thermography principles. This paper presents the key insights and limitations of the modeled thermographic inspections and validates the model with experimental data.

**Keywords:** Thermography, solar loading, non-destructive testing, finite-elements modeling, phase thermography, civil engineering structures, Cultural heritage

### 1. Introduction

Multiple non-destructive testing (NDT) techniques have been used to investigate structures and cultural heritage buildings for defects and internal cavities (or voids), including ground penetrating radar and ultrasonic testing [1]. One of the most currently used techniques is infrared thermography, which has been used to locate hidden elements in walls of cultural heritage buildings, as described in [2]. The experiment described in this article used a heat gun to create a temperature difference. Still, the approach of using an artificial heat source does not apply to the inspection of large surfaces. This is where the technique of solar-loading thermography can be useful.

As its name implies, solar-loading thermography relies on the sun as a heat source to create temperature contrasts between sound areas and 'defective' areas on an inspected surface. These temperature variations are monitored by an infrared camera for a certain period. This technique is useful for inspecting large surfaces without using an active heating source, making it especially useful for the inspection of buildings and large structures. For example, it was used in 2010 to inspect the wall of a building on the campus of Université Laval, and a church in Italy damaged by an earthquake [3]. It has also been applied successfully for the inspection of other cultural heritage monuments, combined with a hybrid approach aiming to retrieve the depth of the investigated defects [4]. Other use cases of solar loading thermography include the inspection of concrete structures to detect delamination under the surface [5] and the detection of defects in wind turbine blades [6, 7].

However, even if multiple articles present case studies of infrared thermography and discuss the influence of experimental parameters and signal processing techniques, few articles have explored the numerical modeling of solar loading thermography observations. Notably, Pozzer et al. [4] modeled a concrete sample with delamination under its surface in COMSOL and monitored the evolution of its surface temperature with a simulated solar heating cycle. However, the goal of this article was to determine the best periods of the year to detect defects under the concrete, with the simulated defects being located 5 cm or less under the surface. The detection of defects was based on thermal gradients, meaning that the defects could be detected in less than a day of observation. The authors of the study presented in [7] also modeled a section of a wind turbine blade with finite element modeling (FEM) software to validate their experimental results and to assess how environmental conditions such as cloud cover and air temperature influence the detectability of simulated defects. Globally, both articles focused on the detection of defects by the temperature contrast generated on the inspected surface and did not process the simulated data using advanced signal processing techniques such as phase thermography, as in article [3].

To the best of our knowledge, there is no study or simulation focused on the detection of deep defects using solar loading thermography, which would require advanced signal processing and multiple days of observation. This paper aims to simulate the temperature variation of a surface subjected to solar radiation by FEM over a long period, using lock-in thermography. The model will be validated by comparing it to experimental data, and further numerical results will show the potential and the limitations of solar loading thermography in terms of the maximum depth of detectable defects over longer periods of observation.



**Fig. 1** Photo of the wall of the Vachon building inspected in article [3]. The area of interest is outlined by a black rectangle.

## 2. Methodology

The type of observation to be done with an infrared camera in solar loading thermography for long periods of observation is based on the principle of modulated or 'lock-in' thermography [9]. This inspection method relies on a periodically modulated energy source heating the material to be inspected. As its name implies, the sun is the energy source in solar loading thermography. An infrared camera monitors the surface temperature, and data is processed by applying a 1D fast Fourier transform (FFT) algorithm to the sequence of recorded thermograms, from which it is possible to obtain phase images or phasegrams. The phase contrast within this image may reveal the presence of defects [10]. If the processed data covers a long period, low frequencies are available, making it possible to view deeper defects, since there is an inverse relationship between the modulation frequency and the probing depth, the lower the frequency the deeper it can reach.

### 2.1 Model Validation

To validate the numerical model, data acquired in 2015 on the southern wall of the Vachon building at Université Laval (see Figure 1), using the same methodology as in [3], was compared to data from a numerical model reproducing this experiment. A wall cross-section was modeled in COMSOL, with the geometry shown in Figure 2 a). The model simulates part of the structure outlined by the black dotted rectangle in Figure 1. It was originally planned to build a bridge between the Vachon building and the neighboring building, but the idea was abandoned. The door where this bridge would have gone through was sealed, resulting in a section of the wall being thinner than its surroundings, and creating a void inside the wall. In the experimental results, this void influences the surface temperature, making it a good reference to verify how close the simulated results are to the experimental results.

To optimize calculation time in the FEM model, only a corner of the door area was modeled, to take advantage of the symmetry of the structure. The surface material is limestone, with a thickness of 12 cm. Under the limestone, in the sound area, the other materials are mortar (2.5 cm thick) and cellular concrete (24 cm thick) From the interior surface, the materials are plaster (2 cm thick) and polyurethane (5 cm thick), covering both the cellular concrete and the void area. The materials and their thickness were taken from the original architectural plans of the building, with the knowledge that polyurethane was added to the envelope in later renovation works. The thermal properties of the materials were mostly taken from [3], and the properties of polyurethane were taken from [11]. They are shown in Table 1. The precise thermal properties of the material used for the Vachon building are unknown, adding uncertainty to the simulation. The conductivity for limestone was adjusted slightly downwards from the source mentioned in [3] (from 2.2 W/m K to 1.8 W/m K) to get a better fit between the simulated data and the experimental data.

**Table 1:** Thermal properties of the materials used for the numerical simulations.

Material	k (W/m K)	$\rho$ , (kg/m <sup>3</sup> )	$c_p$ (J /kg k)
Limestone	1.8	2000	851
Mortar	0.85	3100	840
Cellular concrete	0.3	1050	525
Polyurethane	0.025	30	1400
Plaster	0.5	1440	800
Concrete	1.8	2300	880

The solar radiation and ambient temperature values were calculated using the NSRDB database [12], which includes hourly solar radiation and temperature data for multiple locations around the world. As the database only includes solar irradiation for a horizontal surface, the solar irradiation for a vertical surface oriented toward the southeast, as the southern wall of the Vachon building, was calculated using Eq. (1).

$$P_{sol}(t) = DNI(t) * \cos(\alpha(t)) + DHI(t)/2, \quad \alpha < 90^\circ \quad (1)$$

where DNI(t) is the time-dependent direct normal irradiation, in W/m<sup>2</sup>,  $\alpha(t)$  is the time-dependent angle between the normal of surface exposed to solar irradiation and the direction of the direct solar beams. The direction of the direct solar beams was calculated using the elevation and azimuth of the sun as seen from the Vachon building, using the solar position and

intensity calculator (SOLPOS) from the National Renewable Energy Laboratory [13].  $DHI(t)$  is the time-dependent diffuse irradiation on a horizontal surface. In the case of a vertical surface, it was assumed that the incident diffuse irradiation would be half of that incident on a horizontal surface at the same location, as the vertical surface is exposed to approximately half of the sky.

Heat transfer by convection was considered for both the interior and exterior surfaces. On the outside, the convection coefficient was set at  $12.5 \text{ W/m}^2 \text{ K}$ . The sides of the model have a symmetry boundary condition applied, to represent the continuation of the wall and void structures beyond the geometry's boundaries. On the inside surface, the convection coefficient is kept constant at  $8 \text{ W/m}^2 \text{ K}$ , with a constant ambient temperature of  $293 \text{ K}$  indoors. The emissivity of both the outdoor and indoor surfaces is supposed to be  $0.95$ .

The meshing of the model was refined above the void area more than in the other areas, as this represents the region of interest, and the geometry is thinner in this area. The maximum element size was set to be  $0.04 \text{ m}$ , versus  $0.16 \text{ m}$  in the rest of the geometry. The experimental dataset starts at  $11:21 \text{ AM}$  on July 28, 2015, and ends at  $8:35 \text{ AM}$  on August 5, 2015. The simulation starts at  $0:01 \text{ AM}$  on July 20, 2015, to ensure that the internal temperature of the model has reached a realistic distribution, independent from the uniform initial temperature of the model. The time stepping was set at 30 minutes, which allows us to have a good temporal resolution while keeping calculation time relatively low. In the numerical model, the temperature for both the sound area and the void area were extracted from a single point each, both located far enough from the void's boundaries to avoid border effects. In contrast, the real void area and sound area temperatures were calculated by averaging the values of multiple pixels located inside a rectangular region of interest in each area to reduce noise and obtain a value closer to the actual temperature by minimizing spatial variations.

## 2.2 Deep defects modeling

To evaluate the potential of infrared thermography in the detection of deep defects, another COMSOL model was created. The geometry, seen in Figure 2a), represents a vertical concrete surface with synthetic defects embedded inside, shown in figure 2 b). The model represents a thick section of a concrete wall, with two rows of synthetic defects embedded inside. The thermal properties of the concrete material are shown in the last row of Table 1. The first row has defects of size  $0.80 \text{ m} \times 0.80 \text{ m} \times 0.5 \text{ m}$ , and the second row has defects of size  $1.20 \text{ m} \times 1.20 \text{ m} \times 0.5 \text{ m}$ . Both rows feature six defects, with depths from the surface being  $0.50, 0.75, 1.00, 1.25, 1.50,$  and  $1.75 \text{ m}$ . Defects have a horizontal distance of at least  $4 \text{ m}$  between each other to make sure that their thermal signature does not overlap with each other. The concrete slab is oriented perpendicularly towards the south, with time-dependent solar irradiance being calculated in consequence. The ambient temperature data and solar irradiation are considered for a simulation taking place in Quebec City, in 2022. This year was chosen as this is the most recent year for which solar irradiation data is available. The total duration of the simulation, starting on January 1, 2022, was 600 days. Weather data from 2022 was employed for both years. The first year of the simulation is used to reach a permanent regime for the temperature distribution inside the sample, as its initial temperature is assumed to be constant. This means that datasets starting from March 1, 2022, start 424 days after the simulation start date.

The physics and boundary conditions of the model are mostly the same as those of the experimental validation model, with a key difference, i.e. a symmetry boundary condition is applied to the face opposite to the one exposed to solar irradiation in addition to the sides of the model, to simplify the simulation. The raw surface temperature data of the irradiated face was exported as a  $110 \times 250$  grid, with interpolation being used to have 32 data points for each coordinate per hour, simulating the acquisition of a thermogram sequence at this frequency. The data was then processed using Python programming language. Measurement noise was simulated by adding randomly generated values following a Gaussian distribution (centered at 0, with a standard deviation of  $0.05 \text{ K}$ ) to the whole dataset.

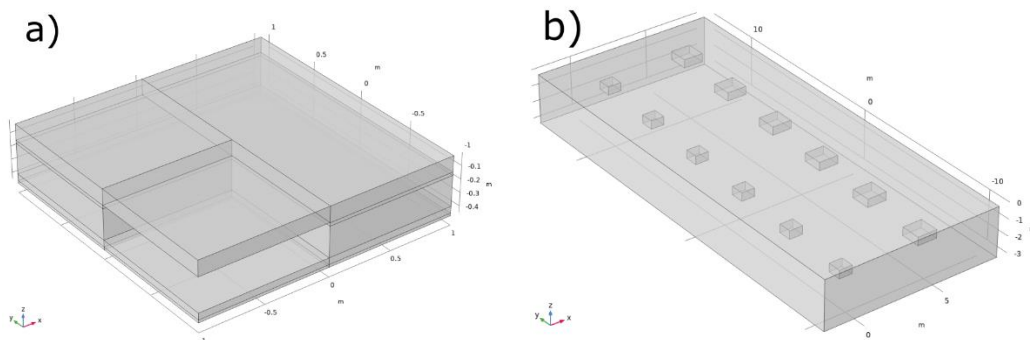
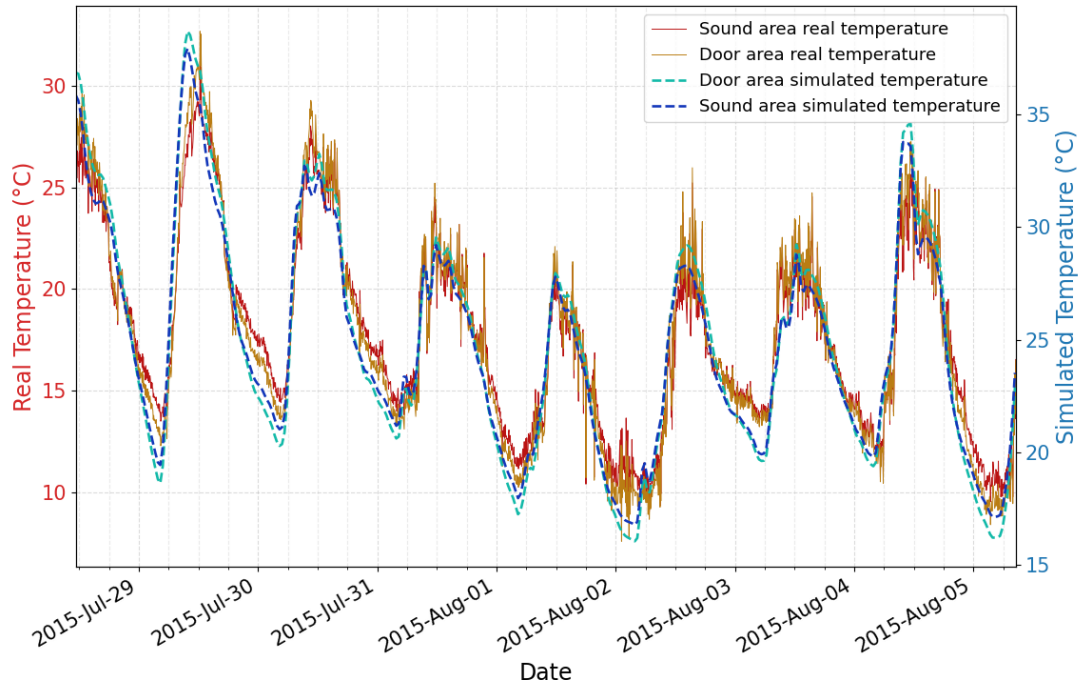


**Fig. 2.** a) Geometry of the model used to validate the experimental data of the Vachon building. b) geometry of the model used to simulate the potential of solar loading for detecting deeper defects.

### 3. Results and Analysis

#### 3.1 Model Validation

The simulated time-dependent surface temperature of the wall cross-section was processed and compared to the real experimental data. The period used for the analysis ranges from July 28, 2015, at 11:21 AM to August 5, 2015, at 8:36 AM, which is the totality of the experimental data. Figure 3 shows the temperature versus time of the door area (also referred to as 'void area') and the sound area for both the experimental (solid lines) and the modeled (dotted lines) data. The left-handed scale shows the temperatures for the real datasets while the right-hand scale shows the temperature for the simulated datasets.



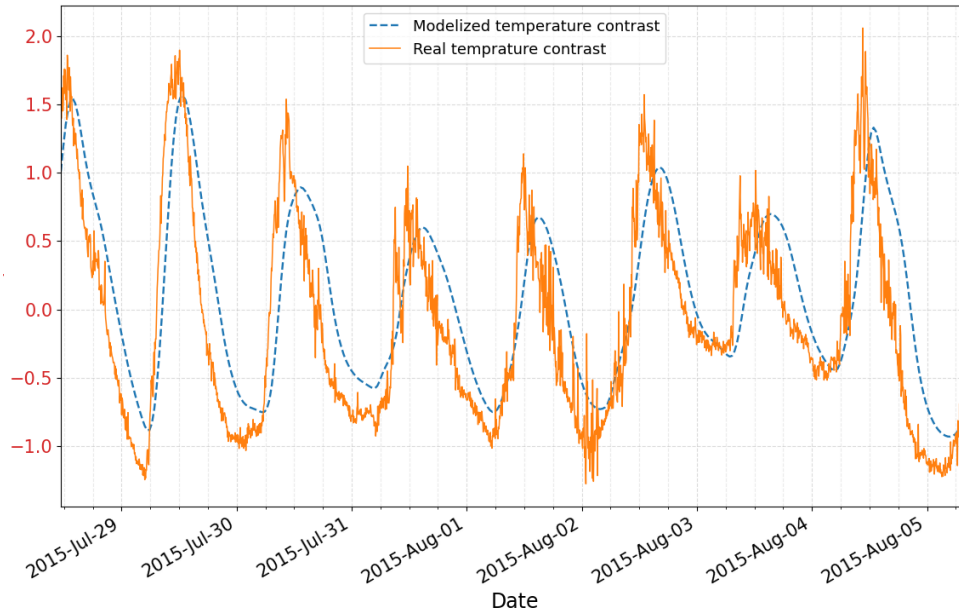
**Fig. 3.** Temperature versus time for the door area (numerical model data and experimental data) and the sound area (numerical model data and experimental data). The scale for the real data is on the left side, and the scale for the modeled data is on the right side.

Figure 3 shows that the real temperature and simulated temperature generally follow the same patterns. For example, days with lower temperature amplitude, like August 1 and August 2, also have a lower amplitude in the simulated dataset. This shows that the model reproduces day-to-day weather variations qualitatively similar by using real ambient temperature and solar irradiation data. It is possible to see greater differences between the real and simulated temperature variations at some points of the data sequence, such as during the first half of July 29, where the simulated temperature drops more steeply before rising more quickly than the real temperature. These slight differences might be caused by factors not considered in the physical modeling, such as the time-dependent variation of the external convection coefficient due to variable wind speed. However, the main difference between the simulated data and the real data is that there is a constant difference between the absolute temperatures of the simulated and real datasets of approximately 8°C.

This constant temperature difference between the numerical and the experimental data is a flaw that has still an unknown cause. It has been tried to change multiple parameters within realistic limits, such as the material thermal properties, the convection coefficients, or the emissivity, but no change has produced better results than those shown in Figure 3. A significant temperature difference between the simulated data and experimental data has also been observed in the article [8], but the temperature difference seen in Figure 3 is larger than that seen in this article.

Figure 4 shows the temperature difference between the void area and the sound area for the experimental data (blue dotted line) and the real data. This figure shows that, while there is a large difference between the absolute temperatures of the real and simulated data, the time-dependent simulated temperature contrast between the void area and the sound area follows the real temperature contrast with great accuracy. Visually, the temperature amplitude of each 34-h cycle is similar for both the real and simulated data. There is a slight phase difference between both datasets and on some days, such as July 29 or July 30, when the temperature contrast becomes negative, the absolute temperature contrast is lower for the simulated data than for the real data.

Applying the FFT algorithm to both the simulated and real datasets makes it possible to calculate the phase contrast between the void area and the sound area for both datasets. When considering the period from July 28, 2015, at 11:21 AM to August 5, 2015, at 8:36 AM, the lowest frequency available in the FFT sequence is approximately  $1.65 \times 10^{-6}$  Hz. At this frequency, the phase contrast between the void area and the sound area is equal to 0.489 radians for the simulated data, compared to 0.496 radians for the real data. This represents an absolute difference of 1.4 %. For higher frequencies, the phase contrast discrepancy between the simulated dataset and the real dataset increases significantly, but for the simulation of solar-loading thermography with deep defects, only the lowest available frequency for each period will be considered.



**Fig. 4.** Time-dependent temperature difference between the sound area and the void area. The curve for the experimental data is the orange line, while the curve for the simulated data is the blue dotted line.

### 3.2 Potential of deep defects detection

The surface temperature data for the thick concrete sample was processed as described in the methodology section. The first period considered for the analysis ranges from March 1, 2022, to April 11, 2022, for 40 days. Figure 5 a) shows a simulated thermogram of the sample's surface at 23:30 on March 1. Figure 5 b) shows the phase image (calculated from the simulated temperature data) for the lowest possible frequency for the period ranging from March 1 to March 30, for a total of 29 days. This subfigure also attributes a number to each defect. Their size and depth are shown in Table 2. All defects have a thickness of 0.5 m.

**Table 2:** Geometry of the synthetic defects embedded in the thick concrete sample.

Defect no.	Cross-section dimension (m)	Depth under the surface (m)	Defect no.	Cross-section dimension (m)	Depth under the surface (m)
1	0.8 x 0.8	0.25	7	1.2 x 1.2	0.25
2	0.8 x 0.8	0.50	8	1.2 x 1.2	0.50
3	0.8 x 0.8	0.75	9	1.2 x 1.2	0.75
4	0.8 x 0.8	1.00	10	1.2 x 1.2	1.00
5	0.8 x 0.8	1.25	11	1.2 x 1.2	1.25
6	0.8 x 0.8	1.50	12	1.2 x 1.2	1.50

The thermogram in figure 5 a) was chosen to be at a time showing the best overall temperature contrasts between the defects and the sound area. We can see that the shallowest defects, no. 1, 2, 7, and 8 are visible, with defects 3 and 9 being visible with a poor contrast. The other defects have a temperature contrast too poor to be visible in this image, especially with the added Gaussian noise. In contrast, the phasegram shown in figure 5 b) shows a visible phase contrast for every defect, even with the same Gaussian being added to the data before processing.

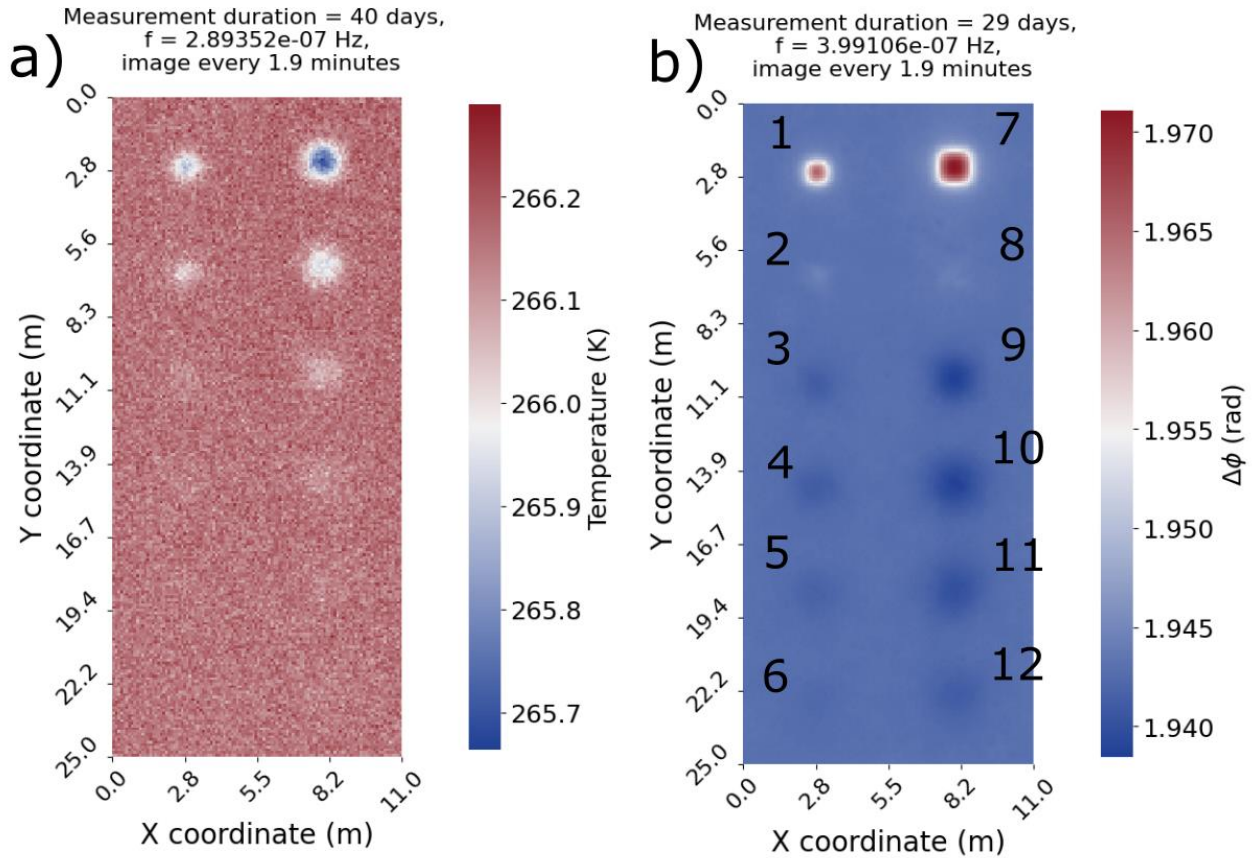


**Fig. 5.** a) Surface temperature of the sample at the simulated time of March 1, 2022, at 23:30. b) Simulated phasegram for a 29-day long observation, taking place from March 1 to March 30, 2022. Defects are numbered from no. 1 to 12.

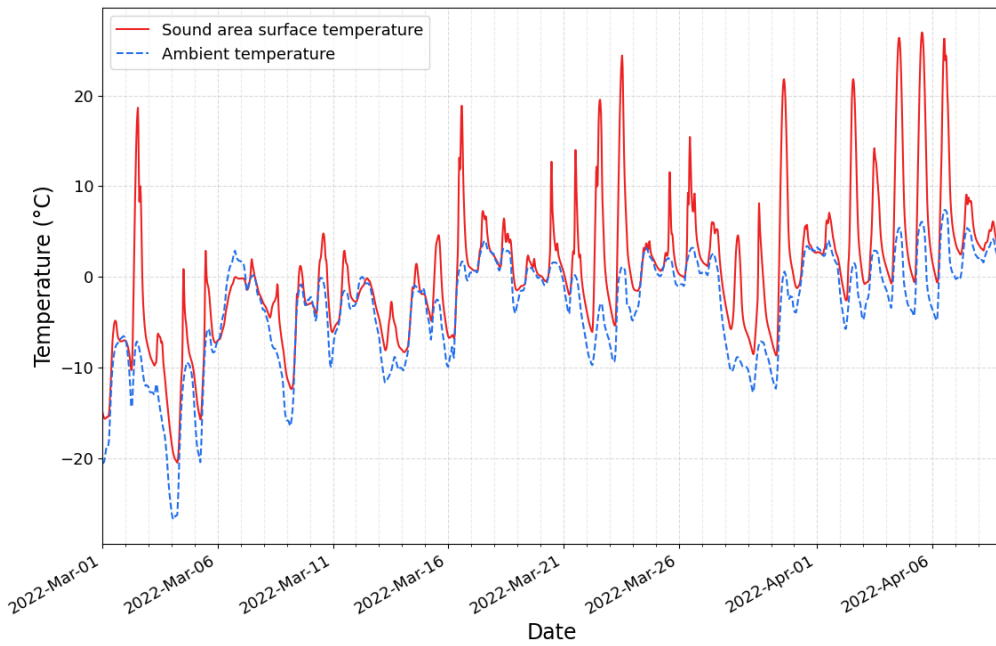
Defect 6, being the hardest defect to detect by its depth and dimensions, is harder to see, but still shows a weak phase contrast. This comparison shows that phase analysis is a powerful processing technique to detect defects located deep under the surface with solar-loading thermography. It is also interesting to note that defects 2 and 8 show a lower phase contrast than all the deeper defects in the sample, except for defect 6. This means that the frequency in figure 5 b) is close to the blind frequency for those two defects. The two shallower defects, no. 1 and 7, both show by far the highest phase contrast in the samples, and have inverted contrast compared to all other defects, this is a sign that the chosen frequency is too low for these particular depths. These observations indicate that, in a sample with features located at multiple different depths, it is hard to estimate the depth of each feature using a single image. Phasegrams at different frequencies, corresponding to the blind frequency of each specific depth, should be used to estimate the different depths.

Figure 6 shows the temperature variation of a random point on the sample's sound area, together with the ambient temperature variation. The surface temperature is generally higher than the ambient temperature, with few exceptions throughout the whole observation period. The ambient temperature acts as a minimum threshold under which surface temperature can not decrease at any given time. Each day, around noon, the surface temperature peaks, as it is at this moment that the incident solar irradiation is the highest. The curves show that the input signal heating the surface is far from a perfect sinusoidal wave generally used in lock-in thermography, complicating the analysis.

To facilitate a quantitative analysis of the results, it is useful to introduce the notion of CNR, or Contrast to Noise Ratio. The CNR can be calculated for a given defect with Eq. (2).

$$CNR = \frac{|S_a - S_n|}{\sigma_n} \quad (2)$$

where  $S_a$  is the mean signal of the area of interest,  $S_n$  is the mean signal of the background or sound area, and  $\sigma_n$  is the standard deviation of the sound area or the level of background noise. For each defect, the area of interest was defined as a rectangle of 3 x 3 pixels centered on the defect. A thin strip in the middle of the sample, with a width of 5 pixels and a height of 50 pixels, serves as a reference for the background signal and noise level.



**Fig. 6.** Surface temperature and Ambient temperature variations between March 1 and April 10

The CNR ratio can be calculated for every defect in each phasegram. For 40 days of measurements, it is possible to compute 40 phasegrams of the lowest available frequency covering different durations. For example, a phasegram covering only the data of the first day of measurement would have a lowest frequency of  $1.15 \times 10^{-5}$  Hz, a phasegram covering the first two days of measurement would have a lowest frequency of  $5.57 \times 10^{-6}$  Hz, and so on. This means lower frequencies should be visible in the first phasegrams produced in a survey, while deeper defects would become visible later.

A compact way to visualize how visible certain defects become depending on the number of days elapsed since the beginning of a survey is to plot their CNR ratio in a phasegram image versus the number of days of data since the survey start date used to make the phasegram. For the dataset ranging from March 1 to April 10, Figure 7 shows the CNR versus time for the six shallowest defects (no. 1, 2, 3, 7, 8, and 9) while Figure 8 shows the CNR versus time for the six deepest defects (no.4, 5, 6, 10, 11 and 12). For this article, we will consider that a defect is visible if its CNR is greater than 2.

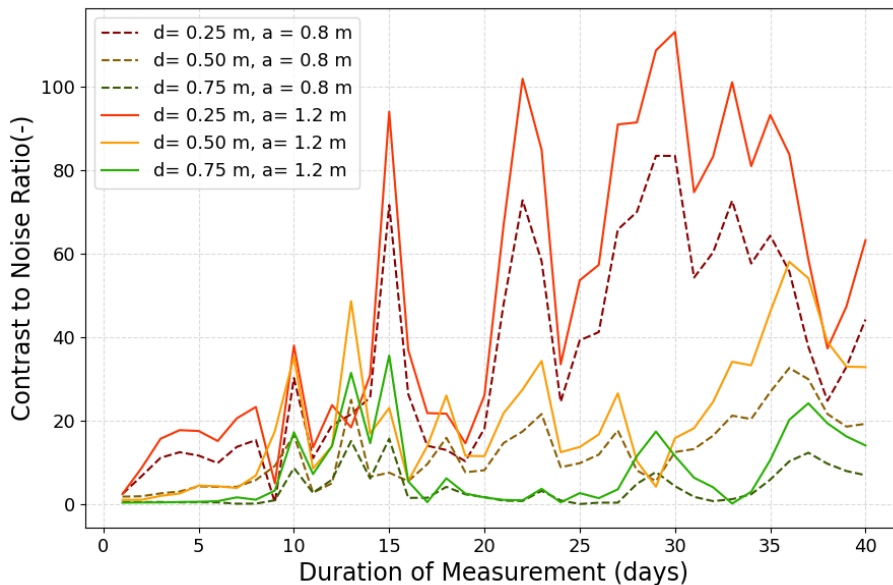


**Fig. 7.** CNR ratio for shallower defects (depth  $d$  between 0.25 m and 0.75 m under the surface) versus the number of days elapsed since the beginning of the survey (March 1, 2022)

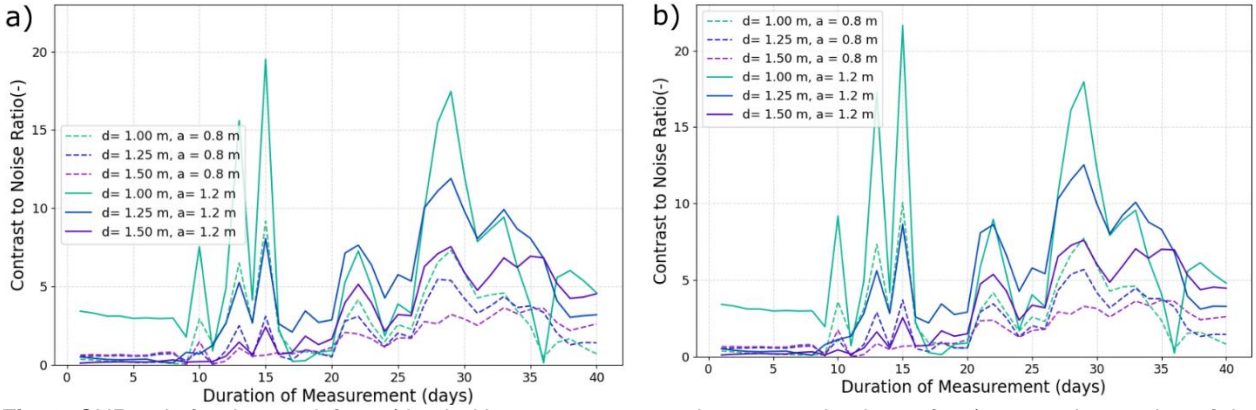


**Fig. 8.** CNR ratio for deeper defects (depth  $d$  between 1.00 m and 1.50 m under the surface) versus the number of days elapsed since the beginning of the survey (March 1, 2022). a) with 0.03 mK Gaussian noise added to the data. b) with no noise added to the data.

In figure 7, we can see that nearly all defects have a good enough CNR to be detected from the first day of the survey. In general, as the measurement duration becomes longer, the CNR of each defect increases, but the relation between those two variables is not trivial. In both figure 7 and 8, the CNR for all defects can vary widely from day to day and can even go from above the detectability threshold to below it in one day. Between day 15 and day 16, the CNR for all defects goes down drastically before going back up quickly after day 20. These seemingly random variations may find an explanation for the influence of day-to-day variations on the survey's results. As shown in Figure 6, the ambient temperature and solar irradiation acting as the input signal are far more complex than 'pure' waves used in lab testing, or the single solar cycles used in most solar-loading studies. These weather variations may have a significant influence on the phasegrams produced from solar-loading thermography data.

In article [3], it is mentioned that there exists an empirical equation to estimate the depth  $d$  of a defect, shown in Eq. (3):

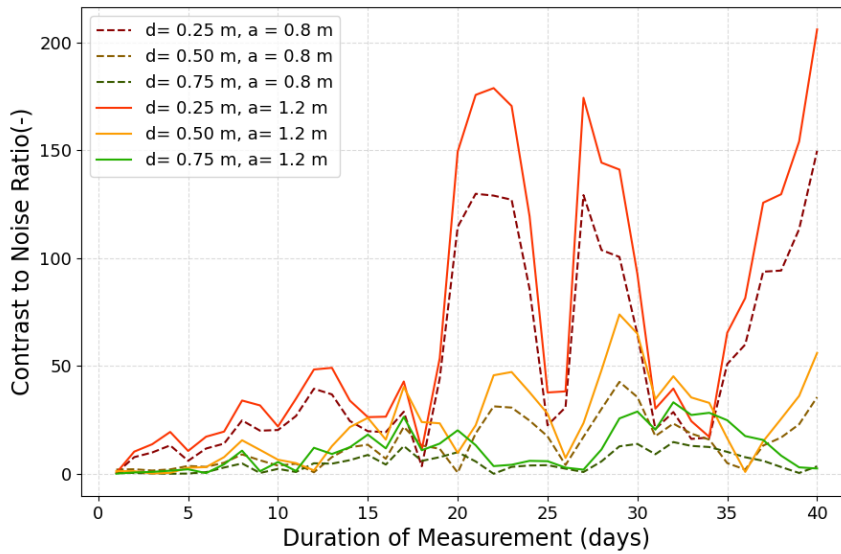
$$d = C_1 \sqrt{\frac{\alpha}{\pi * f_b}} \quad (3)$$

where  $C_1$  is a correlation constant with a value of 1.8 for phase images,  $\alpha$  is the thermal diffusivity constant and  $f_b$  is the blind frequency, which is the frequency at which a defect produces a phase contrast large enough to be detected.  $\alpha$  is the thermal conductivity over the product of specific heat capacity and density. For the concrete used in the simulation, this gives a value of  $\alpha = 8.89 \times 10^{-7} \text{ m}^2/\text{s}$ .

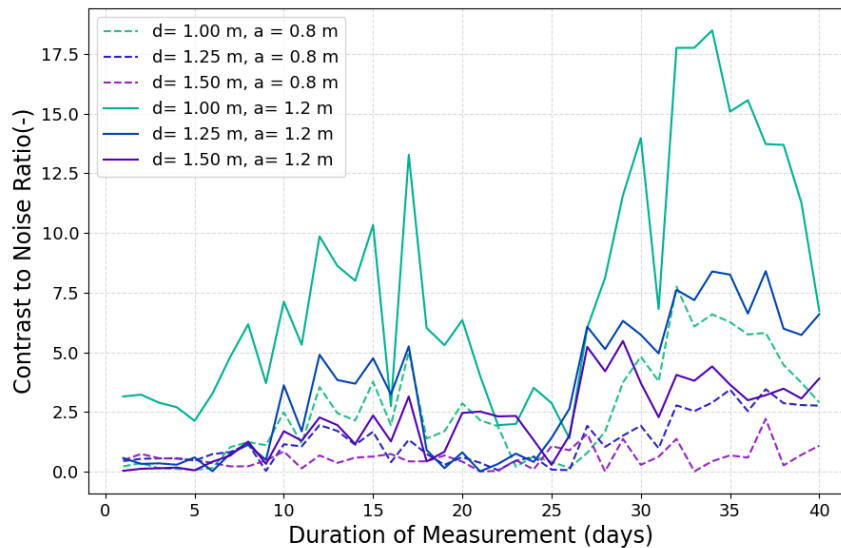
For example, in Figure 8, defects 12 and 6, located 1.5 m below the surface, are detected in approximately 20 and 26 days, respectively. Their estimated depths using Eq. (3) would be 1.25 and 1.42 m respectively. This amounts to a significant underestimation of the depth of both defects, amounting to a difference of 17 % for defect 12. This underestimation of the defect's depth is also visible for defects 5 and 11, both located 1.25 m deep, with estimated depths of 1.00 m and 0.96 m respectively. These discrepancies between the estimated depths of the defect using Eq. (3) and the defects' actual depths indicate that this equation may need to be adjusted when it is used to estimate deeper defects. The comparison between figure 8 a), with Gaussian noise added to the data before pre-processing, and figure 8 b), with no noise added, shows that the synthetic Gaussian noise does not cause this disparity. The CNR ratio in the datasets with no added noise is slightly higher overall than in the datasets with added noise, but the number of days needed to detect is the same in both scenarios.

Figure 9 and Figure 10 show the CNR versus time elapsed since the survey start date, the same way as Figures 7 and 8, but the datasets used for figures 9 and 10 range from June 1, 2022, to July 11, 2022, three months later than the first dataset. It is interesting to note that the curves for all defects in figures 9 and 10 look significantly different than the curves in Figures 7 and 8, even if both datasets have the same duration. The variations of the CNR are not the same in both datasets, and the CNR for defects reached lower values in the dataset starting on June 1. This is more visible when looking at the deepest defects. For example, in the dataset starting on March 1, defect 12 becomes visible after approximately 21 days, while this same defect never surpasses the detectability threshold in the dataset starting on March 1. This observation further reinforces the idea that weather variations may have a large influence on the CNR ratio and detectability of defects when using solar-loading thermography over longer periods.

If this issue is left unaddressed, this may limit the potential uses of long-term solar-loading thermography for the detection of deep defects, as it would be hard to predict with how many days of observation a potential defect at a given depth may become detectable, or if it would be detectable at all during the survey timeframe.



**Fig. 9.** CNR ratio for shallower defects (depth  $d$  between 0.25 m and 0.75 m under the surface) versus the number of days elapsed since the beginning of the survey (June 1, 2022)



**Fig. 10.** CNR ratio for deeper defects (depth  $d$  between 1.00 m and 1.50 m under the surface) versus the number of days elapsed since the beginning of the survey (June 1, 2022)

#### 4. Conclusion

In conclusion, the comparison between the simulated data and the numerical data shows that the numerical model enables to predict the detectability of defects in objects exposed to solar irradiance, as in solar loading thermography. A shortcoming of the model is the fact that the numerical model temperatures are constantly higher than those of the experimental data indicating that the model still has an unknown problem that must be solved. However, the simulated temperature contrasts between defective areas and sound areas are close enough to the experimental temperature contrasts, which is the most important metric for detecting defects in material samples, including with the lock-in thermography method. The results for the sample with deeper defects showed the potential of solar loading thermography to detect defects located deep under the surface.

The deepest synthetic defect in the simulation, located 1.5 m under the surface, could be detected with approximately 20 days of observation in the right circumstances. However, the analysis of the CNR ratio versus the duration of the observation showed that the number of days of observation necessary to detect a defect at a given depth varies depending on the period or environmental conditions during which the survey is conducted.

Apart from improving the accuracy of the modeled absolute temperature, future works could include doing experimental thermographic surveys on structures with known defects at greater depths than the void in the tested Vachon building, to validate the finding of the model's predictions for the detection of deep features. It would also be of great importance to do an in-depth analysis of the environmental factors influencing the detectability of defects when using solar-loading thermography over periods longer than 24 hours. This could include, for example, a statistical tool to estimate the probability of detecting a defect at a given depth in less than a given number of days of observation, depending on the location and time of the year when the measurement is made.

### Acknowledgments

The Social Sciences and Humanities Research Council (SSHRC) of Canada and the Canada Research Chair are thanked for their financial support of this work.

### References

- [1] Moropoulou, Antonia, et al. "Non-destructive techniques as a tool for the protection of built cultural heritage." *Construction and Building Materials* 48 (2013): 1222-1239.
- [2] Glavaš, Hrvoje, et al. "Locating hidden elements in walls of cultural heritage buildings by using infrared thermography." *Buildings* 9.2 (2019): 32.
- [3] Ibarra-Castanedo, Clemente, et al. "Solar loading thermography: Time-lapsed thermographic survey and advanced thermographic signal processing for the inspection of civil engineering and cultural heritage structures." *Infrared Physics & Technology* 82 (2017): 56-74.
- [4] Sfarra, S., et al. "The hybrid thermography approach applied to architectural structures." *Optics for Arts, Architecture, and Archaeology VI*. Vol. 10331. SPIE, 2017.
- [5] Pozzer, Sandra, et al. "Passive infrared thermography for subsurface delamination detection in concrete infrastructure: Capabilities." *Construction and Building Materials* 419 (2024): 135542.
- [6] Worzewski, Tamara, et al. "Thermographic inspection of a wind turbine rotor blade segment utilizing natural conditions as excitation source, Part I: Solar excitation for detecting deep structures in GFRP." *Infrared physics & technology* 76 (2016): 756-766.
- [7] Worzewski, Tamara, Rainer Krankenhagen, and Manoucher Doroshnasir. "Thermographic inspection of wind turbine rotor blade segment utilizing natural conditions as excitation source, Part II: The effect of climatic conditions on thermographic inspections—A long term outdoor experiment." *Infrared Physics & Technology* 76 (2016): 767-776.
- [8] Pozzer, S.; Dalla Rosa, F.; Pravia, Z.M.C.; Rezazadeh Azar, E.; Maldague, X. Long-Term Numerical Analysis of Subsurface Delamination Detection in Concrete Slabs via Infrared Thermography. *Appl. Sci.* 2021, 11, 4323. <https://doi.org/10.3390/app11104323>
- [9] Busse, G., Wu, D., Karpen, W.: Thermal wave imaging with phase sensitive modulated thermography. *J. Appl. Phys.* 71(8), 3962–3965 (1992).
- [10] Wu, D., Karpen, W., & Busse, G. (1992, July). Lockin thermography for multiplex photothermal nondestructive evaluation. In *Proceedings of the QIRT Conference, Paris, France* (pp. 7-9).
- [11] Table 6 Thermal Conductivity, Specific Heat Capacity and Density, [https://help.iesve.com/ve2021/table\\_6\\_thermal\\_conductivity\\_specific\\_heat\\_capacity\\_and\\_density.htm](https://help.iesve.com/ve2021/table_6_thermal_conductivity_specific_heat_capacity_and_density.htm)
- [12] NSRDB: national Solar Radiation Database, <https://nslrdb.nrel.gov/data-viewer>
- [13] National Renewable Energy Laboratory (NREL), <https://midcdmz.nrel.gov/solpos/solpos.html>